Heliyon 10 (2024) e40078

Contents lists available at ScienceDirect

Heliyon

journal homepage: www.cell.com/heliyon

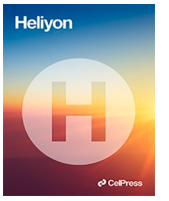

Research article

Hexagonal boron nitride fibers as ideal catalytic support to experimentally measure the distinct activity of Pt nanoparticles in CO_2 hydrogenation

Tímea Hegedűs [a], Imre Szenti [a,b], Anastasiia Efremova [a], Ákos Szamosvölgyi [a], Kornélia Baán [a], János Kiss [a,b], Zoltán Kónya [a,b,*]

[a] *Interdisciplinary Excellence Centre, Department of Applied and Environmental Chemistry, University of Szeged, Rerrich Béla tér 1, H-6720, Szeged, Hungary*

[b] *HUN-REN-SZTE Reaction Kinetics and Surface Chemistry Research Group, Rerrich Béla tér 1, H-6720, Szeged, Hungary*

ARTICLE INFO

Keywords:
h-BN fiber
CO_2 hydrogenation
Catalytic activity
XPS
DRIFTS

ABSTRACT

Catalytic studies aim to design new catalysts to eliminate unwanted by-products and obtain 100 % selectivity for the preferred target product without losing activity. For this purpose, understanding the role of each component building up the catalyst is essential. However, determining the intrinsic catalytic activity of pure metals, especially precious metals in the CO_2 hydrogenation reaction under ambient conditions is complex. This is because the catalyst supports used thus far always influence the catalytic process either directly or indirectly due to interface formation that modifies the electronic and morphological structure of the metals. Even SiO_2, regarded as inert shows some activity owing to the hydroxyl groups on its surface. In this work, we propose chemically inert and defect-free hexagonal boron-nitride fibers (BNF) synthesized via a co-precipitation method with wide band gap and robust covalent bonds as an uncommon reference catalyst support to evaluate the catalytic activity of size-controlled Pt nanoparticles (4.7 ± 0.6 nm) in the hydrogenation of CO_2. The fibers alone show no catalytic activity; however, Pt/BNF exhibited low but notable activity of 377 nmol/g at 400 °C and the catalyst can achieve nearly 100 % CO selectivity. X-ray photoelectron spectroscopy, transmission electron microscopy, and diffuse reflectance infrared Fourier transform spectroscopy measurements were used to indicate that hexagonal boron-nitride affects neither the metal nanoparticles nor the reaction itself; the measured catalytic activity stems from the activity of Pt deposites without the effect of the support, as they were alone. CO vibration spectroscopy studies suggest that due to the lack of substrate-metal interaction, Pt nanoparticles adopt an ideal spherical structure, resulting in several low coordination sites capable of CO_2 conversion. Thus, BNF is proposed in the present article to be used as a reference catalyst support material. It can be efficiently used in investigations involving the proposed metal and reaction or under varying conditions with different metal nanoparticles and reaction systems.

* Corresponding author. Interdisciplinary Excellence Centre, Department of Applied and Environmental Chemistry, University of Szeged, Rerrich Béla tér 1, H-6720 Szeged, Hungary.

E-mail address: konya@chem.u-szeged.hu (Z. Kónya).

https://doi.org/10.1016/j.heliyon.2024.e40078
Received 8 August 2024; Received in revised form 24 October 2024; Accepted 31 October 2024
Available online 5 November 2024

1. Introduction

The constantly growing concentration of greenhouse gases, including CO_2 is a major global problem. To address this ecological concern, scientists employed heterogeneous catalysis [1,2], where the catalytic reaction between H_2 and CO_2 using various catalyst materials is a prominent way for its utilization. As a renewable carbon source, CO_2 turns into useful C1 fuels and its impact on the environment is reduced [3–7]. During heterogeneous catalysis on metal nanoparticles, the metal-support interfaces greatly influence catalytic activity and material properties as a result of interface formation [8]. This phenomenon is termed metal-support interaction (MSI) [9], the combination of the metal-oxide system was recognized to influence the selectivity of the catalysts [10], therefore the investigations regarding these interfaces and their connection to the outcome of the catalytic reaction are important. For example, Pt nanoparticles (Pt NPs) are often applied on oxide supports and the noticeable electronic interaction with the oxide assigned to the MSI [11].

Pt catalysts were utilized in many industrially important reactions over the past including the above-mentioned CO_2 hydrogenation to CO or different hydrocarbons. On a clean Pt(111) surface, the activation of CO_2 with H_2 proceeds through the RWGS mechanism leading to CO production via HOCO intermediate. The HOCO intermediates were determined by DFT calculations on a Pt single crystal. At the same time, further hydrogenation of the transiently formed CO to CH_4 can be observed, happening through a C-O bond cleavage mechanism [12–14]. DFT was primarily used to model the electrochemical reduction of CO_2 on a Pt(111) surface [13]. According to DFT calculations, Pt NPs alone without support do not exhibit activity in CO_2 hydrogenation. Even though the Pt nanoparticles possess active, low-coordinated sites, they are still not able to catalyze the reaction owing to the weak binding of CO_2 to the catalyst. The majority of the works were carried out on Pt supported on oxidic supports [15,16]. When using supported Pt nanoparticles, the CO_2 is stabilized, therefore enhanced activity can be detected; compared to Pt(111) their the superior on oxide supports has been recognized as the effect of low-coordinated sites on small nanoparticles and the large electronic perturbation with the oxide support. On SiO_2 support the observed low activity is caused by OH group formation [12]. Therefore, the investigation of the effective catalytic performance of Pt NPs is challenging, as there is no available data due to the lack of inert oxide-free support.

In these investigations, h-BN as an inert material can be employed as a catalyst support. Defect-free h-BN can serve as inert catalyst support in catalytic research. Naturally, if measurable interaction exists on a vacancy-rich h-BN abundant in defects, it is essential for improving the catalytic activity. The h-BN activation can happen in two ways. Firstly, during the treatment of h-BN with oxygen above 800 °C, boron and nitrogen vacancies are formed [41–43] or secondly, activation can also be done during edge hydroxylating using a steam activation process under conditions above 530 °C [32,44]. It was observed that h-BN sheets rich in vacancies and defects can serve to anchor and also to modify supported metals. In these cases, the catalytic performance is increased due to the metal−support interaction effects [42,45]. The catalytic activity was increased by high temperature (1100 °C) air treatment of a Pt/h-BN nanosphere producing a mild oxidation surface, BNNPsOx [43]. Under these circumstances, however, the charge distribution at the surface was greatly altered compared to the unoxidized sample. In a recent study, the catalytic activity of Ru nanoclusters as a catalyst was investigated on the h-BN nanosheets support in the hydrogenation reaction of aromatic amines [17]. Boron nitride consists of a group compounds with alternatively linked boron and nitrogen atoms with a 1:1 stoichiometry, consisting of B and N atoms in a honeycomb-like configuration, with strong covalent bonds connecting the atoms. When compared to graphene with similar structure but C-C covalent bonds it can be noticed that in the case of h-BN the variation of the electron distribution differs between the atoms. The nitrogen atom has a higher electronegativity and therefore it is attracting the electrons more strongly [18–21]. Notably, BN demonstrates exceptional properties, like chemical inertness, thermal stability and thermal conductivity. Defect-free h-BN exhibits minimum metal–support interaction when compared to conventionally used oxide supports. Due to these properties, Rh-Ni nanoclusters are easily formed on a BN surface as the metal particles are able to migrate freely on the surface and leading to increase the activity in CH_4 reforming with CO_2 [30]. A moderate surface area is observed in the case of low crystalline h-BN. This can preserve their unique characteristics. Coke formation and metal–support interaction are absent, therefore they do not deactivate the Pt/h-BN catalyst for example in the catalytic oxidative decomposition of volatile organic compounds (VOC) [46]. In light of these results and considerations, the activity and the elementary steps of the reaction mechanism in the CO_2 hydrogenation on Pt nanoparticles using size-controlled Pt NPs dispersed on the synthesized high surface area h-BN fibers (BNF) can be established.

As a consequence of the interesting electronic and chemical properties, different forms of h-BN were applied in several technological operation in the recent years. Due to the distinctive properties of h-BN it can act as a template in the case of various atoms, molecules, metal clusters, and particles [18,22–27]. The corrugated structure (moiré pattern) of a monolayer of h-BN on Rh(111) and Ir(111) was found to be a template for Pt nanoparticles [24–26]. Recent studies have shown that h-BN is an appropriate candidate for an oxide-free catalyst support. The adsorption and selective oxidation of oxygen on Au nanoclusters (Au_{55}) on an inert h-BN surface was investigated [28]. The transformation of ethanol on an Au/h-BN/Rh(111) interface exhibited high selectivity, and the product was “CO free” hydrogen, because this way the ethanol dissociates to hydrogen and acetaldehyde without further decomposition [29]. Additionally, in recent studies h-BN alone or with metal nanoparticles on its surface was shown to be efficiently used in selectively catalyzing the oxidative dehydrogenation of propane or other partial oxidation reactions [30–32]. h-BN materials were used as active catalysts in the oxidative dehydrogenation of propane (ODHP) owing to their superior stability in oxidative conditions [31] and also to their high thermal conductivity [33]. The reaction happens without the addition of a metal catalyst [34–38]. Studies also refer to the partial oxidation of methane reforming for CO_2 remediation and simultaneous production of valuable products such as syngas or hydrogen. BN with a Rh-Ni catalyst was effectively applied in dry reforming of methane [30]. Rh supported on h-BN [39] and Ni nanoparticles [40] in another recent study showed high activity and stability towards partial oxidation of methane to syngas.

During the establishment of the reaction path of the reaction of CO_2 with H_2 on Pt nanoparticles previous works were considered. It was suggested by DFT calculations that during the reaction different products are formed, including CO, CH_3OH, and CH_4 [12]. One of

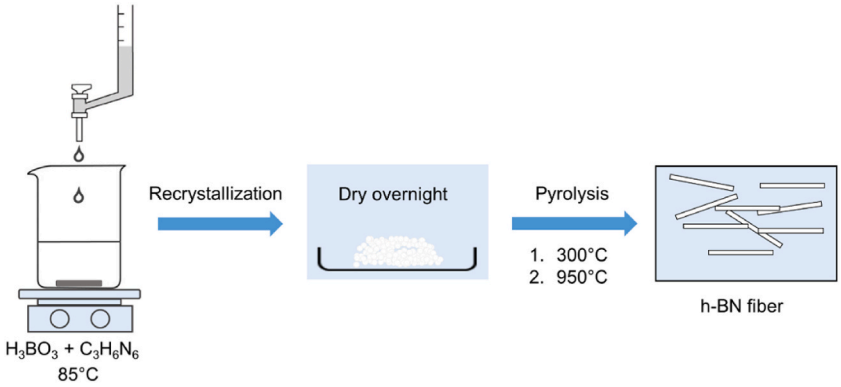

Fig. 1. Schematic representation of the BNF preparation steps.

the main conclusions from these calculations is that low-coordinated sites of Pt nanoparticles are the favorable binding sites for all absorbed species, namely on the corners and the edges. Previous theoretical and experimental studies stated that H_2 dissociates on Pt occurred at a lower temperature than CO_2 hydrogenation takes place. Accordingly, the dissociation of H_2 on the Pt NPs is easy. Therefore, we can conclude that the Pt nanoparticle catalysts are supported on oxides and they can behave differently from Pt (111) [7,8,47–54].

The present study aims to provide a method to determine the catalytic activity of size-controlled Pt NPs alone without the effect of the support under catalytic conditions. The BNF was produced via a co-precipitation method, the material was characterized, and tested as catalyst support with Pt nanoparticles in the CO_2 hydrogenation. The activities were compared with the same size distributed Pt nanoparticles on SiO_2, Co_3O_4, and MnO_2 oxide supports.

2. Materials and methods

2.1. Materials and synthesis

2.1.1. Materials

For the synthesis of BNF and size-controlled Pt NPs melamine ($C_3H_6N_6$), boric acid (H_3BO_3), $H_2PtCl_6{\cdot}xH_2O$, NaOH, polyvinylpyrrolidone (PVP, $M_w = 40000$), ethylene glycol, ethanol and hexane were used. The chemicals obtained from Sigma-Aldrich were used without further purification.

2.1.2. Synthesis of BNF

Different morphological configurations of h-BN can be synthesized [55–58]. Fullerene-like BN nanospheres exhibit zero-dimension, and BN nanotubes and fibers have 1D symmetry. Furthermore, 2D nanosheets and 3D nanoporous h-BN can be synthesized as well [59]. The nanofibers have high surface area, which is also important in catalysis, therefore this morphology has been chosen for detailed investigations.

The BNF was prepared as previously reported [34], with some modifications. The process of the synthesis is schematically presented in Fig. 1. To obtain a concentration of 0.16 mol/dm^3 and 0.08 mol/dm^3, boric acid and melamine were dissolved in distilled water, respectively [60]. Then, the boric acid solution was added slowly, dropwise to the melamine solution with intense stirring at 85 °C. The as-obtained mixture was kept at this temperature until a white solid precursor was formed, as the water evaporated and the reaction between the raw materials led to product recrystallization. The white solid was dried overnight at 80 °C in a drying cabinet. The precursor determined to be melamine-diborate ($C_3N_6H_6{\cdot}2H_3BO_3$) [60] (eq. (1)). Subsequently the fiber-like h-BN structure was achieved by a second heat treatment step.

$$H_3BO_3 + C_3N_6H_6 \rightarrow C_3N_6H_6 \cdot 2H_3BO_3 \rightarrow h-BN \quad (1)$$

The precursor was ground in a mortar with a pestle and placed in a quartz boat, which was heated in the center of a tube furnace equipped with a quartz tube. First, the tube was flushed with N_2 to create an inert atmosphere. The precursor was then subjected to a heat treatment at 300 °C with a heating rate of 10 °C/min for 1 h. Once the system cooled down to room temperature, it was raised again to 950 °C with the same heating rate and held for 2 h. The first heating and cooling steps were necessary since thermogravimetric analysis confirmed a major weight loss at around 300 °C. Holding the system at this temperature and then cooling it ensured the proper formation of BNF and provided a better yield compared to the direct heating of the precursor to the final calcination temperature. The whole process was done under the protection of an inert N_2 atmosphere. After the annealing, a white solid was collected from the quartz boat and further characterized.

2.1.3. Synthesis of Pt nanoparticles

Controlled-size Pt nanoparticles with a 4.7 ± 0.6 nm diameter were prepared via the polyol method as reported before with a few

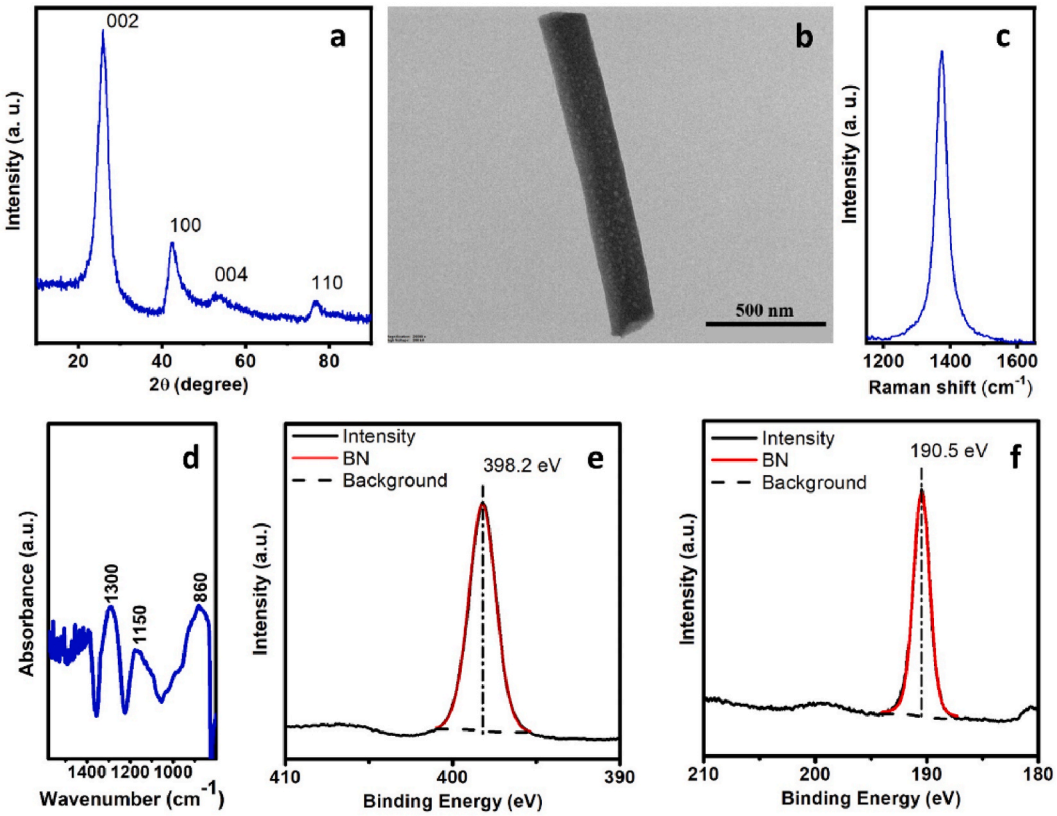

Fig. 2. (a) X-ray diffractogram, (b) TEM image, (c) Raman spectrum, (d) infrared spectrum of the BNF, and high-resolution XPS spectra of (e) N 1s and (f) B 1s regions.

modifications [61]. The Pt precursor, $H_2PtCl_6{\cdot}6H_2O$ (50 mg) and the PVP (220 mg) were dissolved in ethylene glycol (10 mL). The mixture was held at 160° under argon atmosphere for 1 h in an oil bath. The nanoparticles were first precipitated with acetone and centrifuged, then they were repeatedly washed with ethanol and hexane and separated by centrifugation. Finally, the NPs were re-dispersed in ethanol and stored in the refrigerator until further use.

2.1.4. Preparation of the supported metal catalysts

The BNF-supported Pt nanoparticles (Pt/BNF) with a loading of 1 % by weight were formulated via the wet impregnation method. The dispersion of the Pt nanoparticles was mixed with the BNF. The excess solvent was removed and the as-prepared sample was dried overnight at 80 °C.

2.2. Characterization methods of catalysts

The pristine BNF was subjected to XRD measurements using a Rigaku Miniflex II desktop diffractometer with a Ni-filtered Cu-Kα radiation (α = 0.15418 nm) at 40 kV accelerating voltage and 30 mA with a scan speed of 2°/min. Raman spectroscopy was also used to characterize the fibers applying a Bruker Sentera II confocal Raman microscope utilizing laser source of 532 nm wavelength and laser power of 25 mW. The spectral resolution was 4 cm^{-1} using a 50× optical objective and a 50× 1000 μm aperture with 3 coadditions. The sample was measured in solid state on clean glass slides. Using the Brunauer–Emmett–Teller (BET) method the specific surface area of the BNF was determined by employing a Quantachrome NOVA 2200 N_2 gas sorption analyzer at −196 °C. Before the measurements, the samples were pretreated in vacuum (<~0.1 mbar) at 200 °C for 2 h. Inductively coupled plasma (ICP) mass spectrometry was used to quantify Pt NPs utilizing an Agilent Technologies 7700X ICP-MS instrument through tracking the signal of the ^{195}Pt isotope. The samples were dissolved in an acidic solution – composed of HNO_3 and HCl – before the analysis.

TEM analysis of all the catalyst supports (pristine and impregnated with the size-controlled Pt nanoparticles) was carried out with an FEI Tecnai G2 20 X Twin instrument using 200 kV accelerating voltage. The suspensions of the catalysts in isopropanol were drop-casted on amorphous carbon film-coated copper grids with 200 mesh grid density. X-ray photoelectron spectroscopy (XPS) measurements were conducted using a Specs XPS instrument equipped with an XR50 dual anode X-ray source and a Phoibos 150 hemispherical analyzer. The Al Kα X-ray source was operated with 150W (14 kV) power and the charging of the sample was negated using an electron flood gun. Survey spectra were collected with 40eV pass energy and 1eV step size whereas high-resolution spectra were

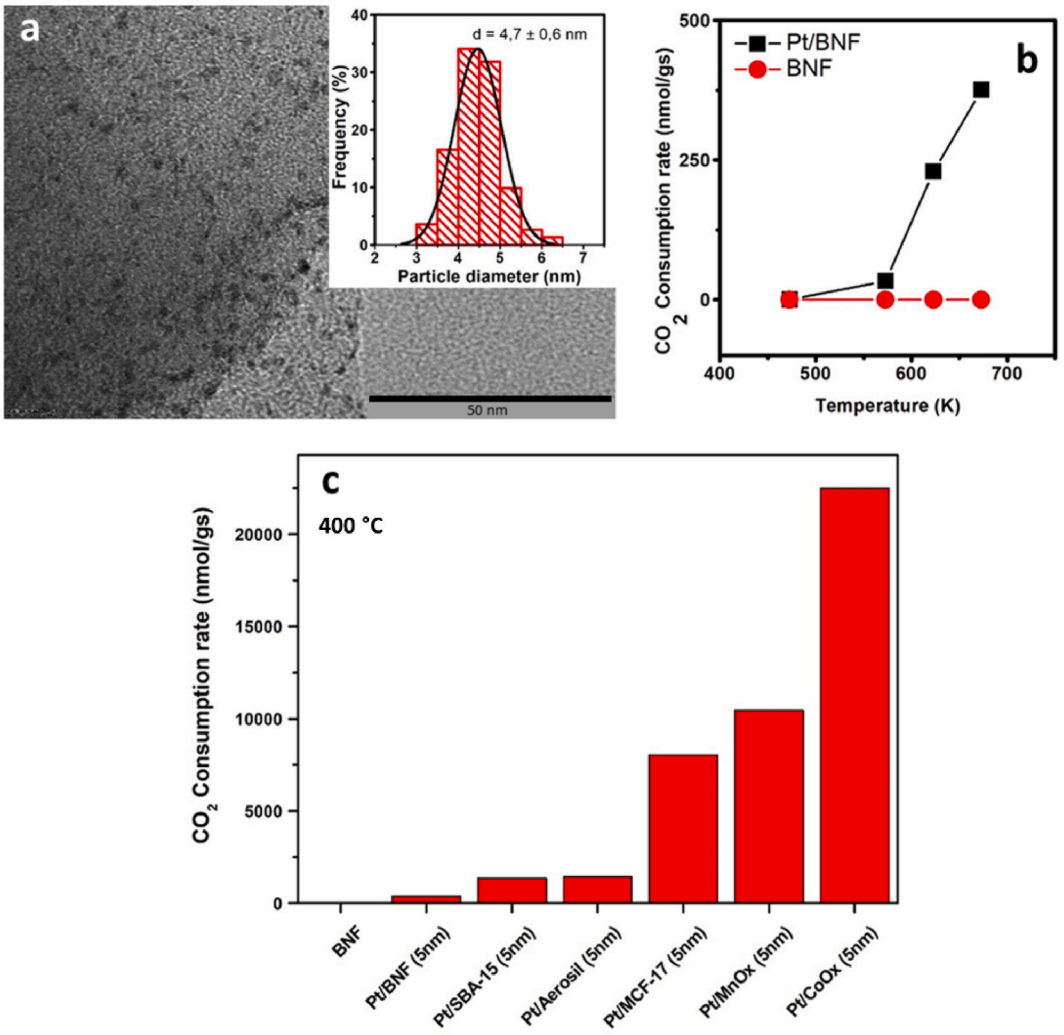

Fig. 3. (a) TEM image of the Pt/BNF made by impregnation (the insert shows size distribution of the Pt NPs), (b) CO_2 consumption rate by temperature (BNF and Pt/BNF), and (c) CO_2 consumption rate of different catalysts.

collected with 20eV pass energy and 0.1eV step size background corrected with a Shirley background. All peaks, except the Pt(0), which is asymmetric, were fitted to a Gauss-Lorentzian product function with the Lorentzian contribution of 30 %. The aliphatic component of the C 1s spectrum region at 284.8 eV was chosen as an inner reference.

DRIFTS measurements were conducted with using a Harrick Praying Mantis diffuse reflectance attachment in an Agilent Cary-670 FTIR spectrometer. The spectrometer was purged with dry nitrogen before the measurement. The background was established using the spectrum of the catalyst that was pretreated and cooled. The measurement started at ambient temperature. The CO_2:H_2 mixture with a molar ratio 1:4 was introduced to the DRIFTS cell at a flow rate of 40 ml/min. The tubes were heated externally to prevent condensation, while the catalyst was heated from room temperature at a rate of 20°/min to 400 °C with the gas mixture being continuously provided. An IR spectrum was recorded at 50 °C intervals.

The samples were tested in the CO_2 hydrogenation under atmospheric pressure in a fixed-bed continuous-flow reactor (200 mm length, 8 mm inner diameter). 100 mg of the sample was placed between quartz wool plugs in the middle of the reactor. Prior to the test reactions the as-received catalysts were pre-treated, the conditions were the same in all experiments unless otherwise noted. The samples were oxidized in an O_2 atmosphere at 300 °C for 30 min followed by reduction in H_2 at 300 °C for 60 min. Pretreatment conditions were the same unless otherwise stated. The temperature was adjusted to the reaction temperature while maintaining the flow of N_2. Then the gas source was exchanged to a mixture of CO_2/H_2 gases at a molar ratio of 1:4 with a constant, 40 mL/min gas flow controlled with the help of mass flow controllers (Aalborg). The products were evaluated using an Agilent 5890 GC equipped with thermal conductivity and flame-ionization detectors (TCD and FID). The CO_2 conversion was calculated by equation (2):

$$CO_2\ Conversion\ (X_{CO2}) = \frac{Moles\ of\ CO_{2in} - Moles\ of\ CO_{2out}}{Moles\ of\ CO_{2in}} \cdot 100 \quad (2)$$

Table 1
The CO_2 consumption rates for the 5 nm Pt nanoparticles on different supports.

Catalyst	CO_2 consumption rate (nmol/gs)	
BNF	0	present article
Pt/BNF	377	present article
Pt/SBA-15	1365	[68]
Pt/Aerosil	1425	Not published data
Pt/MCF-17	8000	Not published data
Pt/MnOx	10465	[68]
Pt/CoOx	22510	[54]

3. Results and discussion

3.1. Characterization of h-BN

Following the above-detailed synthesis method for BNF, the properties and morphological attributes of the synthesized white material were investigated by various techniques. As the structure of h-BN can be effectively defined using XRD measurements by determining the characteristic diffractions, the XRD pattern was observed in the 10–90 2θ degrees range. The diffractogram of the BNF is presented in Fig. 2a, where only the diffractions at positions characteristic of h-BN can be identified, as referenced in the JCPDS file 034–0421. The XRD pattern shows peaks that are well separated at $2\theta = 25.91^\circ$ and 42.35° associated with the (002) and (100) crystallographic planes, respectively [56,62]. Additionally, two other peaks characteristic of h-BN were observed, one at 53.39 2θ value corresponding to the (004) crystal plane, and another at 76.51° representing the (110) crystal plane [56].

The TEM image of the as-synthesized BNF revealed fiber structure with well-defined morphology (Fig. 2b). The average width of the fibers was 182 ± 16.4 nm and their average length was measured as 10 ± 2 μm.

The successful synthesis of BNF was further confirmed by Raman spectroscopy (Fig. 2c). The Raman spectrum displayed a single peak characteristic of the E_{2g} mode associated with h-BN [63]. The infrared spectrum of the clean BNF (Fig. 2d) exhibited features at 870, ~1160, and ~1280 cm^{-1} as reported previously for fullerene-like h-BN nanospheres [56,57], and h-BN nanotubes [64,65]. Observing the 3550-3000 cm^{-1} wavenumber range, the pristine fibers do not contain hydroxyl groups, as no feature attributed to them can be seen. BET measurements revealed a high surface area of 722 m^2/g.

To determine the sample composition and to exclude the presence of impurities, XPS spectroscopy was utilized. The XPS survey spectra showed no signs of contamination. Fig. 2e and f illustrate the high-resolution spectra of B 1s and N 1s, respectively. Two peaks representing boron at 190.8 eV [18,66] and nitrogen at 398.3 eV [18,66] confirm the presence of BN. B 1s at 192.5 eV and O 1s at 532.5 eV for boron oxide were not observed [67]. This confirms that the synthesis protocol leads to the formation of h-BN structures with a fiber-like morphology without contamination.

Further investigations aimed at assessing whether the material is suitable as an inert catalyst support for Pt metal catalysts in the process of hydrogenation of CO_2.

3.2. Catalytic results of Pt/BNF

To demonstrate that BNF can be considered an inert support in the CO_2 hydrogenation reaction, we have used controlled-size Pt nanoparticles previously employed by our research group in combination with various supports in the mentioned reaction under identical experimental conditions [7,50,54,68–71]. The prepared Pt nanoparticles were impregnated onto the BNF support. They were homogeneously distributed over the surface of the support without considerable aggregation, as shown in the TEM images (Fig. 3a). The average metal particle size comprised 4.7 ± 0.6 nm (Fig. 3a insert). It is known from the literature that the Pt nanoparticles are spherically shaped on h-BN [24], whereas on metal [24] or reducible oxide supports such as TiO_2 [72,73] the particle aspect ratio is significantly greater than 1. The Pt loading determined by ICP-MS analysis was ~1 % over the BNF support, therefore the desired loading was achieved by means of the wet impregnation process.

The catalytic activity of the as-prepared catalysts in the CO_2 conversion process was evaluated at ambient pressure over a temperature span of 200–400 °C. The CO_2 consumption rate (nmol/gs) was calculated and is presented in Fig. 3b for both the plain BNF support and the Pt-supported sample. The plain BNF support showed almost no catalytic activity with a negligible CO_2 consumption rate, indicating that CO_2 does not bind to the support without the presence of metal nanoparticles. The Pt/BNF exhibited low catalytic activity towards CO_2 hydrogenation, which improved with increasing the temperature. The CO selectivity remained constant at nearly 100 % throughout the entire temperature range, independent of the temperature.

To get further insight into the behavior of the support and the metal deposits, Fig. 3c presents and compares the CO_2 consumption rates of catalysts prepared by our research group with the same Pt nanoparticles on different supports (SiO_2(Aerosil), SBA-15, MCF-17, MnO_x, CoO_x). It can be observed that the incorporation of Pt nanoparticles on the BNF surface enhances catalytic activity; however, it remains a considerably lower value than that of the same Pt nanoparticles on oxide supports. The data for the CO_2 consumption rates in the case of 5 nm Pt NPs are presented in Table 1. Notably, a lower activity was observed in the case of BNF support than in the case of silica which is mostly considered an inert support material in the literature [5,9,12,74].

An important aspect of catalyst research is the stability of the catalyst. Cyclic stability was assessed at 400 °C and the CO_2

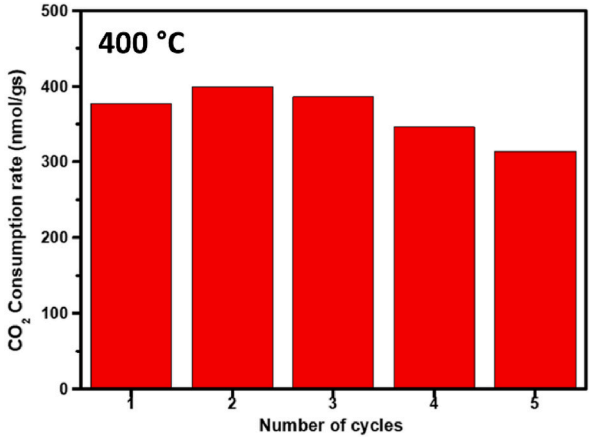

Fig. 4. Stability of the Pt/BNF catalyst in the CO_2 hydrogenation reaction (five cycles).

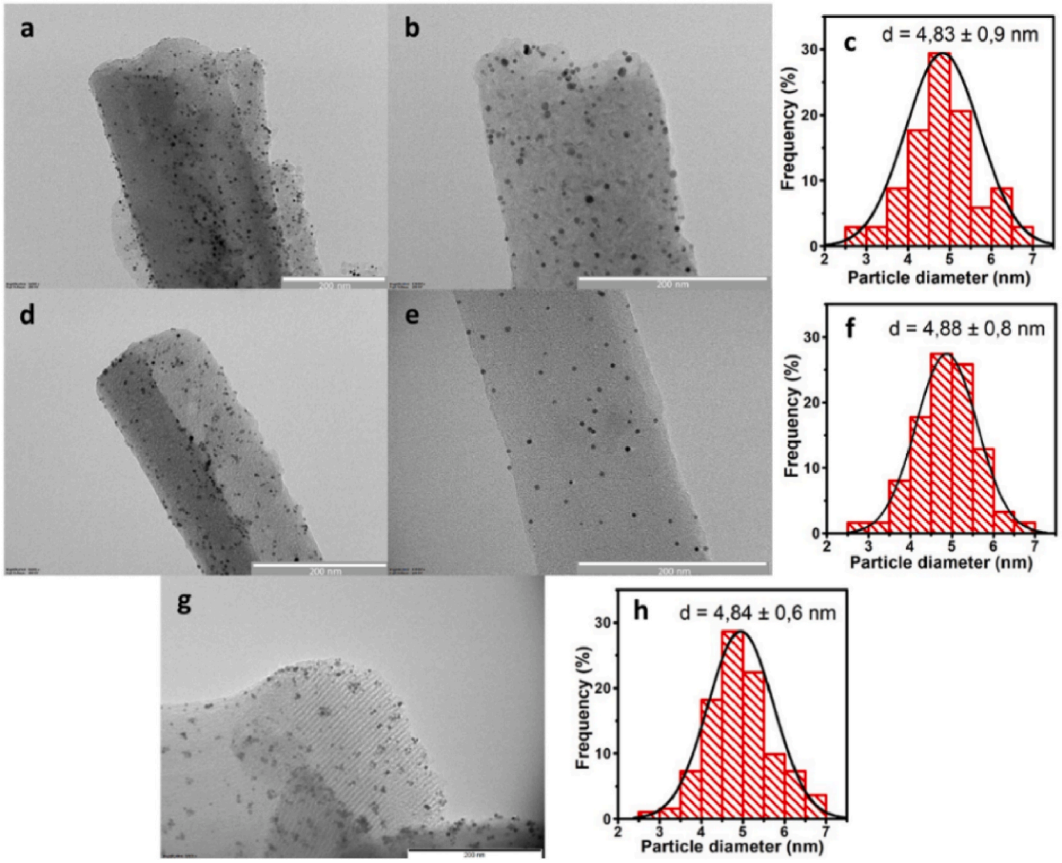

Fig. 5. (a, b) TEM image of Pt/BNF catalyst after the pretreatment, (c) size distribution of the Pt NPs after pretreatment, (d, e) TEM images of Pt/BNF catalyst after catalytic reaction, (f) size distribution of Pt NPs after catalytic reaction, (g) TEM image of Pt/SBA-15 catalyst after the reaction, (h) size distribution of Pt nanoparticles after the reaction on SBA-15.

consumption rate is presented in Fig. 4. In the first cycle the consumption rate was 377 nmol/g. Remarkably, the deviation of the data is within 10 % throughout five cycles. It is concluded that the Pt/BNF catalyst does not suffer significant activity loss in the observed period.

Therefore, we propose that this extremely low activity stems from the inertness of the BNF, resulting from the lack of interactions between the Pt nanoparticles and the BNF. The small activity increase compared to plain BNF can be attributed solely to the catalytic efficiency of the Pt nanoparticles in studied reaction. Based on further results, we aim to explain and confirm this hypothesis in detail.

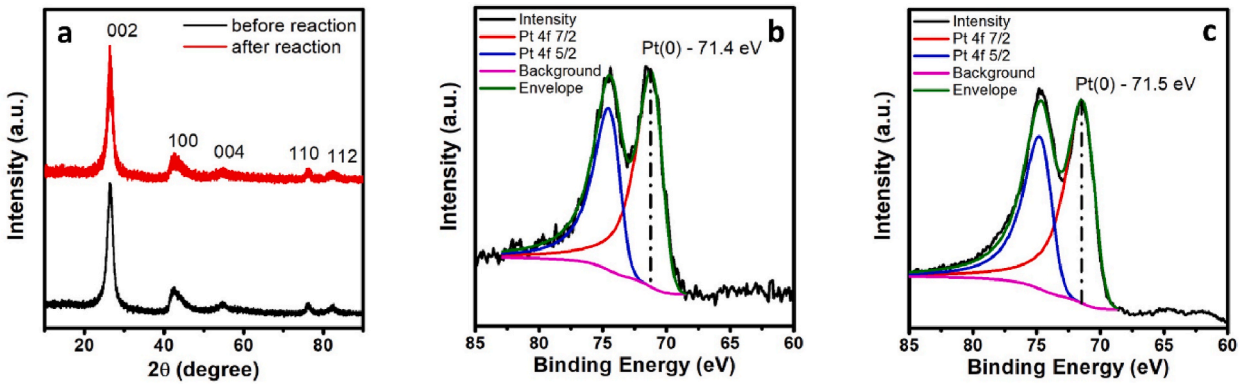

Fig. 6. (a) XRD patterns of the catalyst before and after the reaction, (b) Pt-4f XPS spectrum of Pt/BNF after the reaction, and (c) Pt-4f XPS spectrum of Pt/SBA-15 catalyst after the reaction.

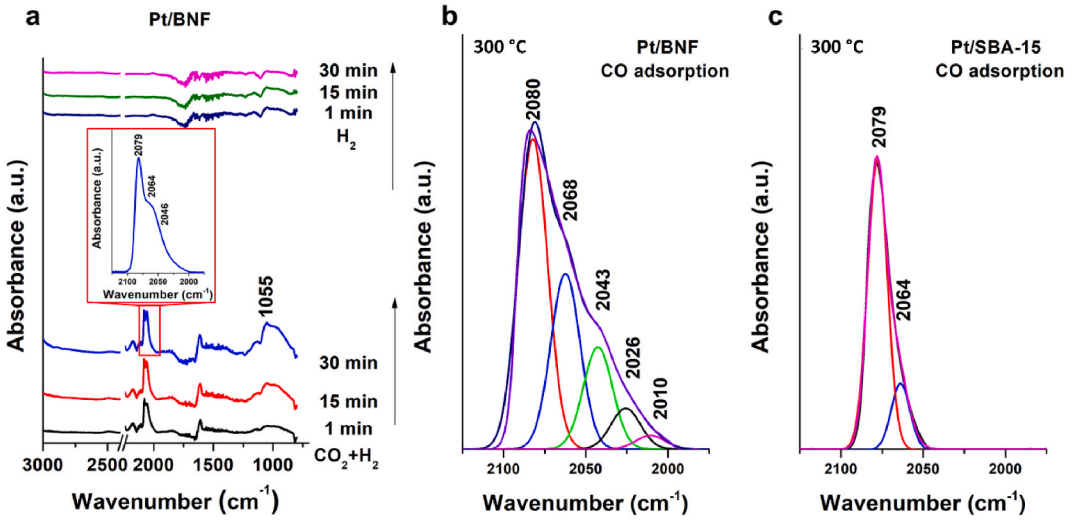

Fig. 7. (a) In situ DRIFTS spectra obtained during CO_2 hydrogenation on Pt/BNF using the BNF spectrum as background; (b) deconvoluted CO spectra obtained during CO adsorption on Pt/BNF, and (c) during CO adsorption on Pt/SBA-15.

3.3. Characterization of the spent catalyst (TEM, XPS, XRD)

To study the behavior of the catalyst and assess whether it suffered any changes during the reaction, additional measurements were conducted. Fig. 5a and b presents the TEM images of the catalyst after pretreatment, while Fig. 5d and e are the TEM images of the catalyst after the CO_2 hydrogenation. The histogram in Fig. 5c displays a size distribution of the Pt NPs on the catalyst support before the reaction, with an average size of 4.83 ± 0.9 nm. After the reaction, the value was measured as 4.88 ± 0.8 nm (Fig. 5f). For comparison, Fig. 5g features an electronic microscopy image of the identical Pt nanoparticles supported on conventional SBA-15, with an average size of 4.84 ± 0.6 nm (Fig. 5h), which is nearly the same as observed on the Pt/BNF. In both cases, spherical morphology was considered [75]. These results indicate that the particles retain their size during the pretreatment and the reaction, compared to the initial size (Fig. 3a). No aggregation and disruption of Pt nanoparticles can be observed in the TEM images and the particles remained evenly distributed in all cases. Observing the TEM images it was noticed that the fiber structure remained and did not suffer degradation under the pretreatment and reaction conditions.

The catalyst was analyzed by XRD both before and after the reaction. In the diffractograms shown in Fig. 6a, the same specific diffractions were observed as described for the BNF support alone (Fig. 2a). Pt was not detected in the diffractograms, likely as they have low loading and high dispersion on the support. Although the diffraction corresponding to the (112) crystallographic plane at 82.1° 2θ was not visible on the XRD pattern of the BNF (Fig. 2a), it is in line with the JCPDS file 034–0421 and other publications on h-BN [76]. This comparison further demonstrates that the BNF support does not undergo any changes during the reaction and its crystalline state remains unaltered.

XPS analysis was carried out to determine the electronic state of the Pt nanoparticles. The Pt-$4f_{7/2}$ signal manifested at 71.4 eV binding energy, which is typical of zero-valent platinum (Fig. 6b). This XPS value was found in our separate experiments in harmony

with the literature-measured value on Pt/SiO_2 [77]. The Pt-4f XP spectral region of Pt/SBA-15 after hydrogen treatment at 300 °C carried out in the same UHV chamber is displayed in Fig. 6c. The same value (71.4–71.5 eV) obtained on both supports indicates no significant charge transfer between Pt and BNF. Similarly, the same binding energy value for Pt-4$f_{7/2}$ was obtained on ~3.4 nm Pt nanocatalyst deposited on h-BN nanomesh formed on Ir(111) [24,26].

3.4. DRIFTS results

In the aim of understanding the interaction between the reactants and the Pt/BNF surface and the mechanism of the catalytic reaction, DRIFT spectra were recorded at increased temperatures in the presence of the reactants and the resulting products. IR spectra obtained during the CO_2 hydrogenation reaction for the Pt/BNF surface are displayed in Fig. 7a.

The identification of IR bands was based on previous vibrational fingerprint data of the species on the surface from prior publications [6,7,71,74,78–82]. On the BNF surface when CO_2 or the mixture of the reactants ($CO_2 + H_2$) were observed, only features at 2400–2200 cm^{-1} and 3750–3550 cm^{-1} (not shown) could be detected owing to CO_2 in the gas state [82]. New reaction species cannot be identified on the clean BNF by DRIFTS. To get a clear picture of the intermediates formed on Pt/BNF catalysts, the clean BNF spectra were used as a background. The spectra were recorded at 300 °C with increasing time and after 30 min the reaction mixture was switched to H_2 stream. When CO_2 and H_2 were added together to the Pt nanoparticles containing surface, new bands started to develop above the temperature of 473 K (Fig. 7a). The intense band around 2080–2040 cm^{-1} was identified as adsorbed CO-related species [8,50,54,79–81]. Another new broad feature forms positioned at 1055 cm^{-1} that corresponds to HOCO, and its intensity increased with reaction time. An IR band around 1600 cm^{-1} was tentatively assigned to water moiety. When the reactant mixture was switched to hydrogen flow, all new peaks formed during the reaction disappeared. One important observation from the IR measurements in terms of establishing the reaction mechanism is that formate or carboxylate intermediates could not be detected. These species are frequent forms in CO_2 hydrogenation when using oxide supports [48,54,71,79,80,83–86]. Along with this, it can be determined that the reaction proceeds via the reversed water gas shift (WGS) reaction mechanism [12]. In this reaction scheme, CO production occurs via a HOCO intermediate [12–14,87]. In the absence of oxide support, there is no possibility of conversion of the HOCO species to carboxylate or carbonates. DFT calculations suggested in the CO_2 hydrogenation process on Pt single crystal the formation of HOCO intermediates. The conversion is exothermic when an activated $*CO_2$ radical turns into an activated *HOCO radical on the surface of the platinum active sites ($\Delta E = -0.09$ eV) with an $E_a = 1.01$ eV. A similar exothermic dissociation can be observed when the formed *HOCO converts to adsorbed CO and OH ($\Delta E = -0.46$ eV), corresponding to $E_a = 0.75$ eV [12]. After that, two possible routes can happen to the CO. It can either desorb from the surface of the metal, or on the other hand it can react with hydrogen that results in the forming of different hydrocarbon fragments. Detecting the HOCO intermediates is challenging, due to its short lifetime, especially in the presence of oxide support. Recently this intermediate was observed by HREELS in water gas shift (WGS) reaction ($H_2O + CO = H_2 + CO_2$) on $Pt_3Ni(111)$. The assessment of the vibrational spectrum reveals the presence of HOCO species at 128–131 meV (approximately 1056 cm^{-1}) [88]. We suspect that this surface complex as an intermediate may exits also at ~1055 cm^{-1} on the Pt/BNF catalyst. The IR peak is quite broad, it has a tailing at the low wavenumber side. One of the explanations for this complex structure is that it contains cis and trans isomers of HOCO. Using an *ab initio* molecular dynamics method in the study of H + HOCO reaction, it was calculated that below 1200 cm^{-1}, the bands of cis and trans isomers together with {HOCOH} intermedier lie between 1111 and 1011 cm^{-1} [89]. We propose that the hydrogen-stabilized HOCO in the {HOCOH} adduct possesses a longer lifetime, making it more straightforward to detect it by in situ DRIFTS techniques. Above 2100 cm^{-1}, the doublet shows the appearance of gas phase CO, indicating the main reaction route. From the DRIFT spectra, we suggest the following reaction mechanism, detailed in eqations 3–5 on BNF-supported Pt catalyst:

$$CO_2 + H_2 \rightarrow {}^*CO_2 + 2H \tag{3}$$

$${}^*CO_2 + H \rightarrow {}^*H - O - C - O \tag{4}$$

$${}^*H - O - C - O \rightarrow CO + OH \tag{5}$$

The activated hydrogen reacts with OH on Pt sites as shown in eqation 6:

$$OH + H \rightarrow H_2O \tag{6}$$

Traces of methane are produced via sequential CO hydrogenation [12–14,47].

Interestingly, the CO IR feature is rather broad, containing at least three main components (Fig. 7a). We suppose that the origin of the CO band shape could either be related to the presence of co-adsorbed hydrogen or it may have morphological reasons. The surface properties of the supported metal nanoparticles by analyzing the adsorbed CO can be effectively investigated by utilizing in-situ DRIFTS spectroscopy [75,90–93]. Therefore, we have separately investigated the adsorption of CO without co-adsorbed hydrogen on the Pt/BNF. The CO adsorption feature after CO adsorption obtained at 200 °C is presented in Fig. 7b. The detailed analysis of absorbed CO DRIFT spectra obtained on a Pt/BNF catalyst shows the same complex feature. In light of a similar result, we conclude that the influence of adsorbed hydrogen on the position of the CO infrared band can be excluded.

The DRIFTS CO adsorption spectra exhibit five well-resolved components. The bands between 2090 and 2000 cm^{-1} are generally attributed to the linearly adsorbed CO [75,90–92]. One peak occurs at 2082 cm^{-1}, moreover one prominent peak appears at 2064 cm^{-1} and three other states appear at low coordination sites, namely at 2046, 2025, and 2009 cm^{-1}. Based on the positions of the peaks

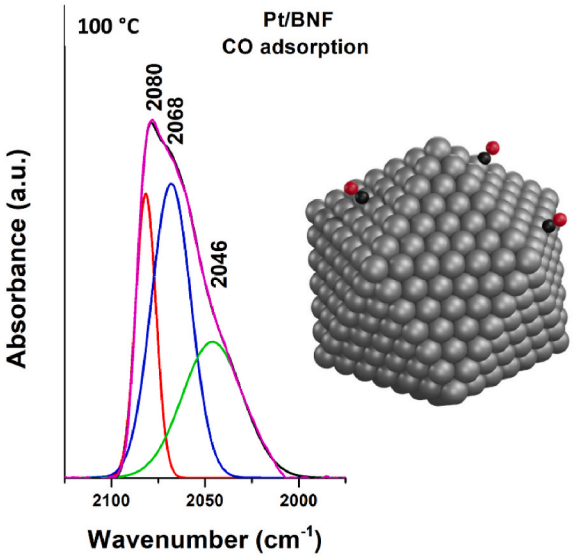

Fig. 8. CO adsorption spectra of Pt/BNF and schematic representation of Pt nanoparticle structure on BNF.

and their intensities, the bridge bonded [75,90,91,93] and gem-dicarbonyl CO species [91,93] can be ruled out. The observed "multiple bands" feature on Pt/BNF is very similar to those obtained during CO adsorption on EuroPt-1 (6.3 wt %Pt/SiO_2) model system at 300 K studied experimentally using DFT calculations [94,95]. Using the notation of the theoretical model regarding the sites [95], we believe that the bands detected when observing the spectra of Pt/BNF can be associated with CO adsorbed on (111) facets of Pt nanoparticles along with edges, corners, and (100) and (110) facets. At the same time, we also take into account the site-specific character of the Pt surface determined recently [96]. It was also demonstrated earlier that the Pt surfaces consisted of (111) terraces interrupted by (110) or (100) monoatomic steps [97]. Additionally, in situ FTIR spectra for full CO coverages on Pt(331) surface with the shortest (111) terraces and (110) steps exhibited a band at 2042 cm^{-1} [96].

This attribute is significantly different from that observed on Pt nanoparticles supported on the quasi-inert support SBA-15. Fig. 7c represents a typical infrared spectrum of CO on Pt nanoparticles supported on SBA-15, reduced at 300 °C and measured in the same experimental system. In harmony with several literature data, the observed strong linear band (2079 cm^{-1}) reflects the homogeneous surfaces of Pt atoms in a spherical form on the catalyst. A tailing at a lower wavelength (2064 cm^{-1}) can be attributed to the minimal coordination (edges, steps) [75,90]. The size, spherical morphology, and oxidation states of Pt atoms on both the BNF and Si support are the same, however, owing to the small interaction in the case of Si with the Pt nanoparticles, less low coordination sites are present [75].

In the lack of significant interactions between Pt metal and support, we believe that the observed feature in adsorbed CO on Pt/BNF can be explained by morphological reasons and the sites developing on the Pt NPs can be accounted for the adsorption forms and reaction mechanism. The proposed active sites in CO_2 hydrogenation are in agreement with the theoretical calculation applied for unsupported Pt nanoparticles in the same reaction [12]. Even though SBA-15 support has less low coordinated sites, the present OH groups, due to the hydroxylated SiO_2 surface, are responsible for the moderately enhanced activity [5,12], which overcompensates the impact of active sites.

The suggested structure of Pt nanoparticles on h-BN fibers, based on CO bands obtained by DRIFTS is schematically represented in Fig. 8. Based on these findings we conclude that the BNF does not contribute to the reaction. That is why it is an ideal support to investigate metal nanoparticles in the CO_2 activation reaction.

4. Conclusion

The use of defect-free hexagonal boron nitride fibers (BNF) enables monitoring the activity and reaction mechanism on metal nanoparticles free from the effect of the support. It is an optimal reference support for investigating the behavior of size-controlled Pt nanoparticles with an initial size of 4.7 ± 0.6 nm in the CO_2 hydrogenation reaction under ambient conditions. The catalytic activity tests showed that the rate of CO_2 consumption on pure BNF was under the detection limit. The Pt-loaded BNF has a higher catalytic activity, it was determined as 377 nmol/g at 400 °C. Besides, the CO selectivity was almost 100 %. TEM images before and after the reaction revealed that the size and spherical shape of the Pt NPs did not change during the reaction. XPS measurements confirmed that the Pt NPs were in the metallic state, with Pt $4f_{7/2}$ binding energy at 71.4 eV both before and after the reaction. DRIFTS experiments demonstrated that the reaction follows a reverse water gas shift reaction mechanism. CO production occurs via a HOCO intermediate which was suggested previously by DFT calculations for Pt single crystal. No carboxylate or formate surface complexes could be detected on the Pt/BNF catalyst.

The topology of Pt NPs was also unfolded by CO adsorption because the infrared bands of adsorbed CO are sensitively influenced by the properties of the active site of the metal component. Analysis of CO vibration states revealed that the ~5 nm Pt nanoparticles were composed of different facets, edges, and corners. Based on our experimental results we concluded that distinct Pt NPs are key factors in the observed catalytic activity without interaction with the support.

The present study confirms that defect-free h-BN serves as an ideal reference support material to investigate the distinct behavior of Pt or other metal nanoparticles in environmentally important reactions like CO_2 hydrogenation or potentially in other catalytic reactions, without the effect of active interface formation between the support material and the metals, especially when the intrinsic activity of the metal nanoparticles is not fully understood.

CRediT authorship contribution statement

Tímea Hegedűs: Writing – original draft, Investigation. **Imre Szenti:** Writing – original draft, Methodology, Conceptualization. **Anastasiia Efremova:** Investigation. **Ákos Szamosvölgyi:** Investigation. **Korbélia Baán:** Investigation. **János Kiss:** Writing – review & editing, Conceptualization. **Zoltán Kónya:** Writing – review & editing, Validation, Supervision, Resources, Funding acquisition, Conceptualization.

Data and code availability

Data will be made available on request.

Declaration of Competing Interest

The authors declare that they have no known competing financial interests or personal relationships that could have appeared to influence the work reported in this paper.

Acknowledgements

The authors acknowledge the contribution of all co-authors in the conceptualization, supervision, investigation, writing editing, and funding process. The authors gratefully thank for the funds of NRDIO OTKA SNN135918, K138714, and Project no. RRF-2.3.1-21-2022-00009, titled National Laboratory for Renewable Energy that has been implemented with the support provided by the RRF of the European Union within the framework of Programme Széchenyi Plan Plus. Supported by the "ÚNKP-23-4-SZTE-554" New National Excellence Program of the Ministry for Culture and Innovation from the source of the NRDIO Fund. This project has received funding from the HUN-REN Hungarian Research Network.

References

[1] G. Centi, E.A. Quadrelli, S. Perathoner, Catalysis for CO_2 conversion: a key technology for rapid introduction of renewable energy in the value chain of chemical industries, Energy Environ. Sci. 6 (2013) 1711–1731, https://doi.org/10.1039/c3ee00056g.

[2] W. Li, H. Wang, X. Jiang, J. Zhu, Z. Liu, X. Guo, C. Song, A short review of recent advances in CO_2 hydrogenation to hydrocarbons over heterogeneous catalysts, RSC Adv. 8 (2018) 7651–7669, https://doi.org/10.1039/c7ra13546g.

[3] R.P. Ye, J. Ding, W. Gong, M.D. Argyle, Q. Zhong, Y. Wang, C.K. Russell, Z. Xu, A.G. Russell, Q. Li, M. Fan, Y.G. Yao, CO_2 hydrogenation to high-value products via heterogeneous catalysis, Nat. Commun. 10 (2019), https://doi.org/10.1038/s41467-019-13638-9.

[4] R.W. Dorner, D.R. Hardy, F.W. Williams, H.D. Willauer, Heterogeneous catalytic CO_2 conversion to value-added hydrocarbons, Energy Environ. Sci. 3 (2010) 884–890, https://doi.org/10.1039/c001514h.

[5] S. Kattel, P. Liu, J.G. Chen, Tuning selectivity of CO_2 hydrogenation reactions at the metal/oxide interface, J. Am. Chem. Soc. 139 (2017) 9739–9754, https://doi.org/10.1021/jacs.7b05362.

[6] T. Rajkumar, A. Sápi, M. Ábel, G. Halasi, J. Kiss, J.F. Gómez-Pérez, H. Bali, Á. Kukovecz, Z. Kónya, Phosphorus-loaded alumina supported nickel catalysts for CO_2 hydrogenation: Ni2P/Ni5P12 drives activity, Mol. Catal. 494 (2020) 1–7, https://doi.org/10.1016/j.mcat.2020.111113.

[7] A. Sápi, T. Rajkumar, M. Ábel, A. Efremova, A. Grósz, A. Gyuris, K.B. Ábrahámné, I. Szenti, J. Kiss, T. Varga, Á. Kukovecz, Z. Kónya, Noble-metal-free and Pt nanoparticles-loaded, mesoporous oxides as efficient catalysts for CO_2 hydrogenation and dry reforming with methane, J. CO_2 Util. 32 (2019) 106–118, https://doi.org/10.1016/j.jcou.2019.04.004.

[8] A. Sápi, T. Rajkumar, J. Kiss, Á. Kukovecz, Z. Kónya, G.A. Somorjai, Metallic nanoparticles in heterogeneous catalysis, Catal. Letters. 151 (2021) 2153–2175, https://doi.org/10.1007/s10562-020-03477-5.

[9] S.J. Tauster, S.C. Fung, R.T.K. Baker, J.A. Horsley, Strong interactions in supported-metal catalysts, Science 211 (1981) 1121–1125, https://doi.org/10.1126/science.211.4487.1121.

[10] S. Kattel, W. Yu, X. Yang, B. Yan, Y. Huang, W. Wan, P. Liu, J.G. Chen, CO_2 hydrogenation over oxide-supported PtCo catalysts: the role of the oxide support in determining the product selectivity, Angew. Chemie. 128 (2016) 8100–8105, https://doi.org/10.1002/ange.201601661.

[11] A. Bruix, J.A. Rodriguez, P.J. Ramírez, S.D. Senanayake, J. Evans, J.B. Park, D. Stacchiola, P. Liu, J. Hrbek, F. Illas, A new type of strong metal-support interaction and the production of H_2 through the transformation of water on Pt/CeO_2(111) and Pt/CeO x/TiO_2(110) catalysts, J. Am. Chem. Soc. 134 (2012) 8968–8974, https://doi.org/10.1021/ja302070k.

[12] S. Kattel, B. Yan, J.G. Chen, P. Liu, CO_2 hydrogenation on Pt, Pt/SiO_2 and Pt/TiO_2: importance of synergy between Pt and oxide support, J. Catal. 343 (2016) 115–126, https://doi.org/10.1016/j.jcat.2015.12.019.

[13] C. Shi, C.P. O'Grady, A.A. Peterson, H.A. Hansen, J.K. Nørskov, Modeling CO_2 reduction on Pt(111), Phys. Chem. Chem. Phys. 15 (2013) 7114–7122, https://doi.org/10.1039/c3cp50645b.

[14] K. Dhar, C. Cavallotti, Investigation of the initial steps of the electrochemical reduction of CO_2on Pt electrodes, J. Phys. Chem. A. 118 (2014) 8676–8688, https://doi.org/10.1021/jp505347k.

[15] X. Chen, Y. Chen, C. Song, P. Ji, N. Wang, W. Wang, L. Cui, Recent advances in supported metal catalysts and oxide catalysts for the reverse water-gas shift reaction, Front. Chem. 8 (2020), https://doi.org/10.3389/fchem.2020.00709.

[16] A.M. Abdel-Mageed, S. Wohlrab, Review of CO_2 reduction on supported metals (alloys) and single-atom catalysts (SACs) for the use of green hydrogen in power-to-gas concepts, Catalysts 12 (2021) 16, https://doi.org/10.3390/catal12010016.

[17] Z. Han, L. Wang, Y. Cao, S. Xu, J. Wu, X. Wang, P. He, H. Liu, Highly dispersed Ru nanoclusters anchored on hexagonal boron nitride for efficient and stable hydrogenation of aromatic amines to alicyclic amines. https://doi.org/10.1021/acs.iecr.3c00985, 2023.

[18] W. Auwärter, Hexagonal boron nitride monolayers on metal supports: versatile templates for atoms, molecules and nanostructures, Surf. Sci. Rep. 74 (2019) 1–95, https://doi.org/10.1016/j.surfrep.2018.10.001.

[19] S. Skarker, Hexagonal boron nitrides (white graphene): a promising method for cancer drug delivery, Int. J. Nanomedicine. 14 (2019) 9983–9993.

[20] Z. Liu, T.B. Marder, B-N versus C-C: how similar are they? Angew. Chemie - Int. Ed. 47 (2008) 242–244, https://doi.org/10.1002/anie.200703535.

[21] R. Gubó, G. Vári, J. Kiss, A.P. Farkas, K. Palotás, L. Óvári, A. Berkó, Z. Kónya, Tailoring the hexagonal boron nitride nanomesh on Rh(111) with gold, Phys. Chem. Chem. Phys. 20 (2018) 15473–15485, https://doi.org/10.1039/c8cp00790j.

[22] Á. Szitás, A.P. Farkas, V. Faur, N. Bera, J. Kiss, Z. Kónya, Investigation of the adsorption properties of cyclic C6 molecules on h-BN/Rh(111) surface, efforts to cover the boron nitride nanomesh by graphene, Surface. Interfac. 32 (2022) 102034, https://doi.org/10.1016/j.surfin.2022.102034.

[23] S. Roy, X. Zhang, A.B. Puthirath, A. Meiyazhagan, S. Bhattacharyya, M.M. Rahman, G. Babu, S. Susarla, S.K. Saju, M.K. Tran, L.M. Sassi, M.A.S.R. Saadi, J. Lai, O. Sahin, S.M. Sajadi, B. Dharmarajan, D. Salpekar, N. Chakingal, A. Baburaj, X. Shuai, A. Adumbumkulath, K.A. Miller, J.M. Gayle, A. Ajnsztajn, T. Prasankumar, V.V.J. Harikrishnan, V. Ojha, H. Kannan, A.Z. Khater, Z. Zhu, S.A. Iyengar, P.A. da S. Autreto, E.F. Oliveira, G. Gao, A.G. Birdwell, M. R. Neupane, T.G. Ivanov, J. Taha-Tijerina, R.M. Yadav, S. Arepalli, R. Vajtai, P.M. Ajayan, Structure, properties and applications of two-dimensional hexagonal boron nitride, Adv. Mater. 33 (2021) 2101589, https://doi.org/10.1002/adma.202101589.

[24] M. Will, T. Hartl, V.B. De La Cruz, P. Lacovig, S. Lizzit, J. Knudsen, T. Michely, P. Bampoulis, Growth, stability, and electronic decoupling of Pt clusters on h-BN/Ir(111), J. Phys. Chem. C 125 (2021) 3880–3889, https://doi.org/10.1021/acs.jpcc.0c10136.

[25] F. Düll, M. Meusel, F. Späth, S. Schötz, U. Bauer, P. Bachmann, J. Steinhauer, H.P. Steinrück, A. Bayer, C. Papp, Growth and stability of Pt nanoclusters from 1 to 50 atoms on h-BN/Rh(111), Phys. Chem. Chem. Phys. 21 (2019) 21287–21295, https://doi.org/10.1039/c9cp04095a.

[26] F. Düll, J. Steinhauer, F. Späth, U. Bauer, P. Bachmann, H.P. Steinrück, S. Wickert, R. Denecke, C. Papp, Ethylene: its adsorption, reaction, and coking on Pt/h-BN/Rh(111) nanocluster arrays, J. Chem. Phys. 152 (2020) 224710, https://doi.org/10.1063/5.0011616.

[27] R. Gubó Szitás, T. Pásztor, A.P. Farkas, T. Ajtai, L. Óvári, K. Palotás, A. Berkó, Z. Kónya, Adsorption of azobenzene on hexagonal boron nitride nanomesh supported by Rh(111), J. Phys. Chem. C 124 (2020) 14182–14194, https://doi.org/10.1021/acs.jpcc.0c01725.

[28] M. Turner, V.B. Golovko, O.P.H. Vaughan, P. Abdulkin, A. Berenguer-Murcia, M.S. Tikhov, B.F.G. Johnson, R.M. Lambert, Selective oxidation with dioxygen by gold nanoparticle catalysts derived from 55-atom clusters, Nature 454 (2008) 981–983, https://doi.org/10.1038/nature07194.

[29] A.P. Farkas, Á. Szitás, D. Jurdi, K. Palotás, J. Kiss, Z. Kónya, Selective transformation of ethanol to acetaldehyde catalyzed by Au/h-BN interface prepared on Rh (111) surface, Appl. Catal. Gen. 592 (2020), https://doi.org/10.1016/j.apcata.2020.117440.

[30] J.C.S. Wu, H.C. Chou, Bimetallic Rh-Ni/BN catalyst for methane reforming with CO2, Chem. Eng. J. 148 (2009) 539–545, https://doi.org/10.1016/j.cej.2009.01.011.

[31] J.T. Grant, C.A. Carrero, F. Goeltl, J. Venegas, P. Mueller, S.P. Burt, S.E. Specht, W.P. McDermott, A. Chieregato, I. Hermans, Selective oxidative dehydrogenation of propane to propene using boron nitride catalysts, Science 354 (2016) 1570–1573, https://doi.org/10.1126/science.aaf7885.

[32] L. Shi, D. Wang, W. Song, D. Shao, W.-P. Zhang, A.-H. Lu, Edge-hydroxylated boron nitride for oxidative dehydrogenation of propane to propylene, ChemCatChem 9 (2017) 1788–1793, https://doi.org/10.1002/cctc.201700004.

[33] J. Tian, J. Lin, M. Xu, S. Wan, J. Lin, Y. Wang, Hexagonal boron nitride catalyst in a fixed-bed reactor for exothermic propane oxidation dehydrogenation, Chem. Eng. Sci. 186 (2018) 142–151, https://doi.org/10.1016/j.ces.2018.04.029.

[34] G. Wang, Y. Yan, X. Zhang, X. Gao, Z. Xie, Three-Dimensional porous hexagonal boron nitride fibers as metal-free catalysts with enhanced catalytic activity for oxidative dehydrogenation of propane, Ind. Eng. Chem. Res. 60 (2021) 17949–17958, https://doi.org/10.1021/acs.iecr.1c04011.

[35] P. Chaturbedy, M. Ahamed, M. Eswaramoorthy, Oxidative dehydrogenation of propane over a high surface area boron nitride catalyst: exceptional selectivity for olefins at high conversion, ACS Omega 3 (2017) 369–374, https://doi.org/10.1021/acsomega.7b01489.

[36] X. Zhang, R. You, Z. Wei, X. Jiang, J. Yang, Y. Pan, P. Wu, Q. Jia, Z. Bao, L. Bai, M. Jin, B. Sumpter, V. Fung, W. Huang, Z. Wu, Radical chemistry and reaction mechanisms of propane oxidative dehydrogenation over hexagonal boron nitride catalysts, Angew. Chemie - Int. Ed. 59 (2020) 8042–8046, https://doi.org/10.1002/anie.202002440.

[37] P. Kraus, R.P. Lindstedt, It's a gas: oxidative dehydrogenation of propane over boron nitride catalysts, J. Phys. Chem. C 125 (2021) 5623–5634, https://doi.org/10.1021/acs.jpcc.1c00165.

[38] J.M. Venegas, Z. Zhang, T.O. Agbi, W.P. McDermott, A. Alexandrova, I. Hermans, Why boron nitride is such a selective catalyst for the oxidative dehydrogenation of propane, Angew. Chemie - Int. Ed. 59 (2020) 16527–16535, https://doi.org/10.1002/anie.202003695.

[39] J. Yao, Y. Xu, H. Yang, Z. Ren, L. Wu, Y. Tang, Identifying the metallic state of Rh catalyst on boron nitride during partial oxidation of methane by using the product molecule as the infrared probe, Catalysts 12 (2022), https://doi.org/10.3390/catal12101146.

[40] Y. Xu, J. Yao, H. Lin, Q. Lv, B. Liu, L. Wu, L. Tan, Y. Dai, X. Zong, Y. Tang, Functional CeOx stabilized metallic Ni catalyst supported on boron nitride for durable partial oxidation of methane to syngas at high temperature, ACS Catal. (2024) 11845–11856, https://doi.org/10.1021/acscatal.4c01055.

[41] Z. Zhang, J. Su, A.S. Matias, M. Gordon, Y.S. Liu, J. Guo, C. Song, C. Dun, D. Prendergast, G.A. Somorjai, J.J. Urban, Enhanced and stabilized hydrogen production from methanol by ultrasmall Ni nanoclusters immobilized on defect-rich h-BN nanosheets, Proc. Natl. Acad. Sci. U. S. A. 117 (2020) 29442–29452, https://doi.org/10.1073/pnas.2015897117.

[42] W. Zhu, Z. Wu, G.S. Foo, X. Gao, M. Zhou, B. Liu, G.M. Veith, P. Wu, K.L. Browning, H.N. Lee, H. Li, S. Dai, H. Zhu, Taming interfacial electronic properties of platinum nanoparticles on vacancy-abundant boron nitride nanosheets for enhanced catalysis, Nat. Commun. 8 (2017) 15291, https://doi.org/10.1038/ncomms15291.

[43] A.M. Kovalskii, I.N. Volkov, N.D. Evdokimenko, O.P. Tkachenko, D.V. Leybo, I.V. Chepkasov, Z.I. Popov, A.T. Matveev, A. Manakhov, E.S. Permyakova, A. S. Konopatsky, A.L. Kustov, D.V. Golberg, D.V. Shtansky, Hexagonal BN- and BNO-supported Au and Pt nanocatalysts in carbon monoxide oxidation and carbon dioxide hydrogenation reactions, Appl. Catal. B Environ. 303 (2022) 120891, https://doi.org/10.1016/j.apcatb.2021.120891.

[44] J. Dong, L. Gao, Q. Fu, Hexagonal boron nitride meeting metal: a new opportunity and territory in heterogeneous catalysis, J. Phys. Chem. Lett. 12 (2021) 9608–9619, https://doi.org/10.1021/acs.jpclett.1c02626.

[45] J. Dong, L. Gao, Q. Fu, Hexagonal boron nitride meeting metal: a new opportunity and territory in heterogeneous catalysis, J. Phys. Chem. Lett. 12 (2021) 9608–9619, https://doi.org/10.1021/acs.jpclett.1c02626.

[46] J.C.S. Wu, Z.A. Lin, J.W. Pan, M.H. Rei, A novel boron nitride supported Pt catalyst for VOC incineration, Appl. Catal. Gen. 219 (2001) 117–124, https://doi.org/10.1016/S0926-860X(01)00673-1.

[47] A. Goguet, F.C. Meunier, D. Tibiletti, J.P. Breen, R. Burch, Spectrokinetic investigation of reverse water-gas-shift reaction intermediates over a Pt/CeO_2 catalyst, J. Phys. Chem. B 108 (2004) 20240–20246, https://doi.org/10.1021/jp047242w.

[48] A. Sápi, U. Kashaboina, K.B. Ábrahámné, J.F. Gómez-Pérez, I. Szenti, G. Halasi, J. Kiss, B. Nagy, T. Varga, Á. Kukovecz, Z. Kónya, Synergetic of pt nanoparticles and h-zsm-5 zeolites for efficient CO_2 activation: role of interfacial sites in high activity, Front. Mater. 6 (2019), https://doi.org/10.3389/fmats.2019.00127.

[49] T. Toyao, S. Kayamori, Z. Maeno, S.M.A.H. Siddiki, K.I. Shimizu, Heterogeneous Pt and MoOx Co-loaded TiO_2 catalysts for lowerature CO_2 hydrogenation to form CH3OH, ACS Catal. 9 (2019) 8187–8196, https://doi.org/10.1021/acscatal.9b01225.

[50] A. Sápi, G. Halasi, J. Kiss, D.G. Dobó, K.L. Juhász, V.J. Kolcsár, Z. Ferencz, G. Vári, V. Matolin, A. Erdőhelyi, Á. Kukovecz, Z. Kónya, In situ DRIFTS and NAP-XPS exploration of the complexity of CO_2 hydrogenation over size-controlled Pt nanoparticles supported on mesoporous NiO, J. Phys. Chem. C 122 (2018) 5553–5565, https://doi.org/10.1021/acs.jpcc.8b00061.

[51] Y. Wang, H. Arandiyan, J. Scott, K.F. Aguey-Zinsou, R. Amal, Single atom and nanoclustered Pt catalysts for selective CO_2 reduction, ACS Appl. Energy Mater. 1 (2018) 6781–6789, https://doi.org/10.1021/acsaem.8b00817.

[52] K. Sun, N. Rui, Z. Zhang, Z. Sun, Q. Ge, C.J. Liu, A highly active Pt/In_2O_3catalyst for CO_2hydrogenation to methanol with enhanced stability, Green Chem. 22 (2020) 5059–5066, https://doi.org/10.1039/d0gc01597k.

[53] E.S. Gutterød, A. Lazzarini, T. Fjermestad, G. Kaur, M. Manzoli, S. Bordiga, S. Svelle, K.P. Lillerud, E. Skúlason, S. Øien-Ødegaard, A. Nova, U. Olsbye, Hydrogenation of CO_2 to methanol by Pt nanoparticles encapsulated in UiO-67: deciphering the role of the metal-organic framework, J. Am. Chem. Soc. 142 (2020) 999–1009, https://doi.org/10.1021/jacs.9b10873.

[54] A. Efremova, I. Szenti, J. Kiss, Á. Szamosvölgyi, A. Sápi, K. Baán, L. Olivi, G. Varga, Z. Fogarassy, B. Pécz, Á. Kukovecz, Z. Kónya, Nature of the Pt-Cobalt-Oxide surface interaction and its role in the CO_2 Methanation, Appl. Surf. Sci. 571 (2022), https://doi.org/10.1016/j.apsusc.2021.151326.

[55] D. Golberg, Y. Bando, Y. Huang, T. Terao, M. Mitome, C. Tang, C. Zhi, Boron nitride nanotubes and nanosheets, ACS Nano 4 (2010) 2979–2993, https://doi.org/10.1021/nn1006495.

[56] T. Hegedűs, D. Takács, L. Vásárhelyi, I. Szilágyi, Z. Kónya, Specific ion effects on aggregation and charging properties of boron nitride nanospheres, Langmuir 37 (2021) 2466–2475, https://doi.org/10.1021/acs.langmuir.0c03533.

[57] L. Vásárhelyi, T. Hegedüs, S. Sáringer, G. Ballai, I. Szilágyi, Z. Kónya, Stability of boron nitride nanosphere dispersions in the presence of polyelectrolytes, Langmuir 37 (2021) 5399–5407, https://doi.org/10.1021/acs.langmuir.1c00656.

[58] A. Pakdel, C. Zhi, Y. Bando, D. Golberg, Low-dimensional boron nitride nanomaterials, Mater. Today 15 (2012) 256–265, https://doi.org/10.1016/S1369-7021(12)70116-5.

[59] X.F. Jiang, Q. Weng, X. Bin Wang, X. Li, J. Zhang, D. Golberg, Y. Bando, Recent progress on fabrications and applications of B4oron nitride nanomaterials: a review, J. Mater. Sci. Technol. 31 (2015) 589–598, https://doi.org/10.1016/j.jmst.2014.12.008.

[60] C. Wu, B. Wang, N. Wu, C. Han, X. Zhang, Y. Wang, In situ molten phase-assisted self-healing for maintaining fiber morphology during conversion from melamine diborate to boron nitride, RSC Adv. 10 (2020) 11105–11110, https://doi.org/10.1039/c9ra10292b.

[61] H. Wang, A. Sapi, C.M. Thompson, F. Liu, D. Zherebetskyy, J.M. Krier, L.M. Carl, X. Cai, L.W. Wang, G.A. Somorjai, Dramatically different kinetics and mechanism at solid/liquid and solid/gas interfaces for catalytic isopropanol oxidation over size-controlled platinum nanoparticles, J. Am. Chem. Soc. 136 (2014) 10515–10520, https://doi.org/10.1021/ja505641r.

[62] C. Tang, Y. Bando, Y. Huang, C. Zhi, D. Golberg, Synthetic routes and formation mechanisms of spherical boron nitride nanoparticles, Adv. Funct. Mater. 18 (2008) 3653–3661, https://doi.org/10.1002/adfm.200800493.

[63] C. Bartus Pravda, T. Hegedűs, E.F. Oliveira, D. Berkesi, Á. Szamosvölgyi, Z. Kónya, R. Vajtai, Á. Kukovecz, Hexagonal boron nitride nanosheets protect exfoliated black phosphorus layers from ambient oxidation, Adv. Mater. Interfaces 9 (2022) 1–8, https://doi.org/10.1002/admi.202200857.

[64] S.H. Lim, J. Luo, W. Ji, J. Lin, Synthesis of boron nitride nanotubes and its hydrogen uptake, Catal. Today 120 (2007) 346–350, https://doi.org/10.1016/j.cattod.2006.09.016.

[65] J. Yu, Y. Chen, B.M. Cheng, Dispersion of boron nitride nanotubes in aqueous solution with the help of ionic surfactants, Solid State Commun. 149 (2009) 763–766, https://doi.org/10.1016/j.ssc.2009.03.001.

[66] L. Bignardi, P. Lacovig, R. Larciprete, D. Alfè, S. Lizzit, A. Baraldi, Exploring 2D materials at surfaces through synchrotron-based core-level photoelectron spectroscopy, Surf. Sci. Rep. 78 (2023) 100586, https://doi.org/10.1016/j.surfrep.2023.100586.

[67] J. Kiss, K. Révész, F. Solymosi, Segregation of boron and its reaction with oxygen on Rh, Appl. Surf. Sci. 37 (1989) 95–110, https://doi.org/10.1016/0169-4332(89)90976-8.

[68] I. Szenti, A. Efremova, J. Kiss, A. Sápi, L. Óvári, G. Halasi, U. Haselmann, Z. Zhang, J. Morales-Vidal, K. Baán, Á. Kukovecz, N. López, Z. Kónya, Pt/MnO interface induced defects for high reverse water gas shift activity, Angew. Chemie. 136 (2024), https://doi.org/10.1002/ange.202317343.

[69] A. Ochirkhuyag, A. Sápi, Á. Szamosvölgyi, G. Kozma, Á. Kukovecz, Z. Kónya, One-pot mechanochemical ball milling synthesis of the MnO: xnanostructures as efficient catalysts for CO2 hydrogenation reactions, Phys. Chem. Chem. Phys. 22 (2020) 13999–14012, https://doi.org/10.1039/d0cp01855d.

[70] A. Sápi, S. Mutyala, S. Garg, M. Yadav, J.F. Gómez-Pérez, F. Czirok, Z. Sándor, K. Hernadi, F. Farkas, S. Kovačič, Á. Kukovecz, Z. Kónya, Size controlled Pt over mesoporous NiO nanocomposite catalysts: thermal catalysis vs. photocatalysis, J. Porous Mater. 28 (2021) 605–615, https://doi.org/10.1007/s10934-020-00978-x.

[71] A. Efremova, T. Rajkumar, Á. Szamosvölgyi, A. Sápi, K. Baán, I. Szenti, J. Gómez-Pérez, G. Varga, J. Kiss, G. Halasi, Á. Kukovecz, Z. Kónya, Complexity of a Co3O4System under ambient-pressure CO_2 methanation: influence of bulk and surface properties on the catalytic performance, J. Phys. Chem. C 125 (2021) 7130–7141, https://doi.org/10.1021/acs.jpcc.0c09717.

[72] A. Berkó, J. Szökő, F. Solymosi, Preparation and reactivity of Rh nanoparticles on TiO2(110)-(1×2) surface, Solid State Ionics 141–142 (2001) 197–202, https://doi.org/10.1016/S0167-2738(01)00845-1.

[73] J.B. Park, S.F. Conner, D.A. Chen, Bimetallic Pt - Au clusters on TiO 2 (110), Growth , Surface Composition , and Metal - Support Interactions 2 (2008) 5490–5500.

[74] A. Erdőhelyi, Hydrogenation of carbon dioxide on supported Rh catalysts, Catalysts 10 (2020), https://doi.org/10.3390/catal10020155.

[75] L. Deng, H. Miura, T. Shishido, S. Hosokawa, K. Teramura, T. Tanaka, Strong metal-support interaction between Pt and SiO_2 following high-temperature reduction: a catalytic interface for propane dehydrogenation, Chem. Commun. 53 (2017) 6937–6940, https://doi.org/10.1039/c7cc03859c.

[76] S. Yuan, B. Toury, C. Journet, A. Brioude, Synthesis of hexagonal boron nitride graphene-like few layers, Nanoscale 6 (2014) 7838–7841, https://doi.org/10.1039/c4nr01017e.

[77] M. Yadav, I. Szenti, M. Ábel, Á. Szamosvölgyi, K.B. Ábrahámné, J. Kiss, P. Zsolt, A. Sápi, Á. Kukovecz, Z. Kónya, Concentrated platinum-gallium nanoalloy for hydrogen production from the catalytic steam reforming of ethanol, ChemCatChem 15 (2023), https://doi.org/10.1002/cctc.202200717.

[78] J. Baltrusaitis, J. Schuttlefield, E. Zeitler, V.H. Grassian, Carbon dioxide adsorption on oxide nanoparticle surfaces, Chem. Eng. J. 170 (2011) 471–481, https://doi.org/10.1016/j.cej.2010.12.041.

[79] Y. Guo, S. Mei, K. Yuan, D.J. Wang, H.C. Liu, C.H. Yan, Y.W. Zhang, Low-temperature CO2 methanation over CeO_2-supported Ru single atoms, nanoclusters, and nanoparticles competitively tuned by strong metal-support interactions and H-spillover effect, ACS Catal. 8 (2018) 6203–6215, https://doi.org/10.1021/acscatal.7b04469.

[80] L. Falbo, C.G. Visconti, L. Lietti, J. Szanyi, The effect of CO on CO_2 methanation over Ru/Al2O3 catalysts: a combined steady-state reactivity and transient DRIFT spectroscopy study, Appl. Catal. B Environ. 256 (2019) 117791, https://doi.org/10.1016/j.apcatb.2019.117791.

[81] K. Zhao, L. Wang, E. Moioli, M. Calizzi, A. Züttel, Identifying reaction species by evolutionary fitting and kinetic analysis: an example of CO_2 hydrogenation in DRIFTS, J. Phys. Chem. C 123 (2019) 8785–8792, https://doi.org/10.1021/acs.jpcc.8b11105.

[82] J.C.S. Wu, C.W. Huang, In situ DRIFTS study of photocatalytic CO_2 reduction under UV irradiation, Front. Chem. Eng. China 4 (2010) 120–126, https://doi.org/10.1007/s11705-009-0232-3.

[83] B. László, K. Baán, E. Varga, A. Oszkó, A. Erdőhelyi, Z. Kónya, J. Kiss, Photo-induced reactions in the CO_2-methane system on titanate nanotubes modified with Au and Rh nanoparticles, Appl. Catal. B Environ. 199 (2016) 473–484, https://doi.org/10.1016/j.apcatb.2016.06.057.

[84] Z. Cheng, C.S. Lo, Mechanistic and microkinetic analysis of CO_2 hydrogenation on ceria, Phys. Chem. Chem. Phys. 18 (2016) 7987–7996, https://doi.org/10.1039/c5cp07469j.

[85] G.N. Vayssilov, M. Mihaylov, P.S. Petkov, K.I. Hadjiivanov, K.M. Neyman, Reassignment of the vibrational spectra of carbonates, formates, and related surface species on ceria: a combined density functional and infrared spectroscopy investigation, J. Phys. Chem. C 115 (2011) 23435–23454, https://doi.org/10.1021/jp208050a.

[86] H.L. Huynh, J. Zhu, G. Zhang, Y. Shen, W.M. Tucho, Y. Ding, Z. Yu, Promoting effect of Fe on supported Ni catalysts in CO_2 methanation by in situ DRIFTS and DFT study, J. Catal. 392 (2020) 266–277, https://doi.org/10.1016/j.jcat.2020.10.018.

[87] Á. Szamosvölgyi, Á. Pitó, A. Efremova, K. Baán, B. Kutus, M. Suresh, A. Sápi, I. Szenti, J. Kiss, T. Kolonits, Z. Fogarassy, B. Pécz, Á. Kukovecz, Z. Kónya, Optimized Pt-Co alloy nanoparticles for reverse water-gas shift activation of CO_2, ACS Appl. Nano Mater. 7 (2024) 9968–9977, https://doi.org/10.1021/acsanm.4c00111.

[88] A. Politano, G. Chiarello, The formation of HOCO in the coadsorption of water and carbon monoxide on Pt3Ni(111), RSC Adv. 4 (2014) 45641–45646, https://doi.org/10.1039/c4ra08066a.
[89] H.-G. Yu, J.S. Francisco, Energetics and kinetics of the reaction of HOCO with hydrogen atoms, J. Chem. Phys. 128 (2008) 244315, https://doi.org/10.1063/1.2946696.
[90] S. Kikkawa, K. Teramura, K. Kato, H. Asakura, S. Hosokawa, T. Tanaka, Formation of CH_4 at the metal-support interface of Pt/Al_2O_3 during hydrogenation of CO_2 : operando XAS-DRIFTS study, ChemCatChem 14 (2022), https://doi.org/10.1002/cctc.202101723.
[91] F. Solymosi, M. Pasztor, An infrared study of the influence of carbon monoxide chemisorption on the topology of supported rhodium, J. Phys. Chem. 89 (1985) 4789–4793, https://doi.org/10.1021/j100268a026.
[92] I.A. Fisher, A.T. Bell, A comparative study of CO and CO_2 hydrogenation over Rh/SiO2, J. Catal. 162 (1996) 54–65, https://doi.org/10.1006/jcat.1996.0259.
[93] Á. Kukovecz, G. Pótári, A. Oszkó, Z. Kónya, A. Erdohelyi, J. Kiss, Probing the interaction of Au, Rh and bimetallic Au-Rh clusters with the TiO_2 nanowire and nanotube support, Surf. Sci. 605 (2011) 1048–1055, https://doi.org/10.1016/j.susc.2011.03.003.
[94] C. Brieger, J. Melke, N. Van Der Bosch, U. Reinholz, H. Riesemeier, A. Guilherme Buzanich, M.K. Kayarkatte, I. Derr, A. Schökel, C. Roth, A combined in-situ XAS-DRIFTS study unraveling adsorbate induced changes on the Pt nanoparticle structure, J. Catal. 339 (2016) 57–67, https://doi.org/10.1016/j.jcat.2016.03.034.
[95] C. Lentz, S.P. Jand, J. Melke, C. Roth, P. Kaghazchi, DRIFTS study of CO adsorption on Pt nanoparticles supported by DFT calculations, J. Mol. Catal. Chem. 426 (2017) 1–9, https://doi.org/10.1016/j.molcata.2016.10.002.
[96] M.J.S. Farias, C. Busó-Rogero, A.A. Tanaka, E. Herrero, J.M. Feliu, Monitoring of CO binding sites on stepped Pt single crystal electrodes in alkaline solutions by in situ FTIR spectroscopy, Langmuir 36 (2020) 704–714, https://doi.org/10.1021/acs.langmuir.9b02928.
[97] B. Lang, R.W. Joyner, G.A. Somorjai, Low energy electron diffraction studies of high index crystal surfaces of platinum, Surf. Sci. 30 (1972) 440–453, https://doi.org/10.1016/0039-6028(72)90011-8.